All-optical routing of single photons by a one-atom switch controlled by a single photon

Itay Shomroni *et al.*

Science **345**, 903 (2014);
DOI: 10.1126/science.1254699

How could the Pacific SST cool when the heat sink was located in other ocean basins? Why didn't the Atlantic SST simply cool as heat was being subducted in its basin? The Atlantic SST and its upper layers did start to cool (Fig. 1B) after its subpolar salinity peaked and then started to decrease after 2006 (Fig. 6A). Before 2006, our warm salt subduction mechanism does not allow the Atlantic to cool when its subpolar salinity was increasing, because poleward transport of warm salty water and increasing subpolar subduction are parts of the same mechanism of enhanced AMOC upper-ocean transport. During this first part of the hiatus period, the heat deficit must be transferred to other ocean basins, mostly to the Pacific because it is the only other major ocean basin in the Northern Hemisphere, likely through the atmosphere. Zhang and Delworth (*45*) and Zhang *et al.* (*46*) showed by using models that, as the northward heat transport by the AMOC is increased, the atmospheric heat transport decreases in compensation (and vice versa), providing a multidecadal component to the Pacific Decadal Oscillation (PDO). The concept behind the flexible atmospheric heat transport is known as nonlinear baroclinic adjustment (*47*). Thus, almost-"synchronized" hemisphere-wide atmospheric changes are possible (*30*). On climate time scales and from an energy perspective, the amount of radiative energy available to heat the global SST, including the Pacific, is what remains after accounting for the energy sink; it does not matter if the latter is located outside the Pacific.

Conclusion

The fact that the global-mean temperature, along with that of every major ocean basin, has not increased for the past 15 years, as they should in the presence of continuing radiative forcing, requires a planetary sink for the excess heat. Although the tropical Pacific is the source of large interannual fluctuations caused by the exchange of heat in its shallow tropical layer (*3*), the current slowdown is in addition associated with larger decadal changes in the deeper layers of the Atlantic and the Southern oceans. The next El Niño, when it occurs in a year or so, may temporarily interrupt the hiatus, but, because the planetary heat sinks in the Atlantic and the Southern Oceans remain intact, the hiatus should continue on a decadal time scale. When the internal variability that is responsible for the current hiatus switches sign, as it inevitably will, another episode of accelerated global warming should ensue.

REFERENCES AND NOTES

1. K. E. Trenberth, J. T. Fasullo, M. A. Balmaseda, *J. Clim.* **27**, 3129–3144 (2014).
2. Intergovernmental Panel on Climate Change, *Summary for Policymakers, Climate Change 2007: Synthesis Report* (Cambridge Univ. Press, Cambridge, 2007).
3. K. E. Trenberth, J. T. Fasullo, *Earth's Future* **1**, 19–32 (2013).
4. K. E. Trenberth, J. T. Fasullo, *Science* **328**, 316–317 (2010).
5. G. A. Meehl, J. M. Arblaster, J. T. Fasullo, A. Hu, K. E. Trenberth, *Nat. Clim. Change* **1**, 360–364 (2011).
6. D. R. Easterling, M. F. Wehner, *Geophys. Res. Lett.* **36**, L08706 (2009).
7. D. Roemmich *et al.*, *Oceanography* **22**, 46–55 (2009).
8. J. M. Lyman, G. C. Johnson, *J. Clim.* **27**, 1945–1957 (2014).
9. J. M. Lyman *et al.*, *Nature* **465**, 334–337 (2010).
10. M. Ishii, M. Kimoto, *J. Oceanogr.* **65**, 287–299 (2009).
11. J. M. Lyman, G. C. Johnson, *J. Clim.* **21**, 5629–5641 (2008).
12. M. Ishii, A. Shouji, S. Sugimoto, T. Matsuoto, *Int. J. Climatol.* **25**, 865–879 (2005).
13. M. Ishii, M. Kimoto, K. Sakamoto, S. I. Iwasaki, *J. Oceanogr.* **62**, 155–170 (2006).
14. C. A. Katsman, G. J. van Oldenborg, *Geophys. Res. Lett.* **38**, L14610 (2011).
15. M. A. Balmaseda, K. Mogensen, A. T. Weaver, *Q. J. R. Meteorol. Soc.* **139**, 1132–1161 (2013).
16. Y. Kosaka, S.-P. Xie, *Nature* **501**, 403–407 (2013).
17. S. T. Gille, *Science* **295**, 1275–1277 (2002).
18. J. R. Toggweiler, J. Russell, *Nature* **451**, 286–288 (2008).
19. R. Zhang, *Geophys. Res. Lett.* **35**, L20705 (2008).
20. J. Jungclaus, H. Haak, M. Latif, U. Mikolajewicz, *J. Clim.* **18**, 4013–4031 (2005).
21. C. Wang, L. Zhang, *J. Clim.* **26**, 6137–6162 (2013).
22. R. Zhang, *Geophys. Res. Lett.* **34**, L12713 (2007).
23. M. H. England *et al.*, *Nat. Clim. Change* **4**, 222–227 (2014).
24. G. A. Meehl, A. Hu, J. M. Arblaster, J. T. Fasullo, K. E. Trenberth, *J. Clim.* **26**, 7298–7310 (2013).
25. I. V. Polyakov, V. A. Alekseev, U. Bhatt, E. I. Polyakova, X. Zhang, *Clim. Dyn.* **34**, 439–457 (2010).
26. H. Hátún, A. B. Sandø, H. Drange, B. Hansen, H. Valdimarsson, *Science* **309**, 1841–1844 (2005).
27. R. Curry, B. Dickson, I. Yashayaev, *Nature* **426**, 826–829 (2003).
28. M. Dima, G. Lohmann, *J. Clim.* **20**, 2706–2719 (2007).
29. M. G. Wyatt, J. A. Curry, *Clim. Dyn.* **42**, 2763–2782 (2014).
30. M. G. Wyatt, S. Kravtsov, A. A. Tsonis, *Clim. Dyn.* **38**, 929–949 (2012).
31. G. Danabasoglu *et al.*, *J. Clim.* **25**, 5153–5172 (2012).
32. P. R. Gent *et al.*, *J. Clim.* **24**, 4973–4991 (2011).
33. S. Solomon *et al.*, *Science* **327**, 1219–1223 (2010).
34. S. Solomon *et al.*, *Science* **333**, 866–870 (2011).
35. B. D. Santer *et al.*, *Nat. Geosci.* **7**, 185–189 (2014).
36. R. K. Kaufmann, H. Kauppi, M. L. Mann, J. H. Stock, *Proc. Natl. Acad. Sci. U.S.A.* **108**, 11790–11793 (2011).
37. B. B. B. Booth, N. J. Dunstone, P. R. Halloran, T. Andrews, N. Bellouin, *Nature* **484**, 228–232 (2012).
38. J. Hansen, M. Sato, P. Kharecha, K. von Schuckmann, *Atmos. Chem. Phys.* **11**, 13421–13449 (2011).
39. G. A. Schmidt, D. T. Shindell, K. Tsigaridis, *Nat. Geosci.* **7**, 158–160 (2014).
40. J. Zhou, K. K. Tung, *J. Clim.* **23**, 3234–3248 (2010).
41. K. K. Tung, J. Zhou, *Proc. Natl. Acad. Sci. U.S.A.* **110**, 2058–2063 (2013).
42. R. Zhang *et al.*, *J. Atmos. Sci.* **70**, 1135–1144 (2013).
43. Z. Wu, N. E. Huang, J. M. Wallace, B. Smoliak, X. Chen, *Clim. Dyn.* **37**, 759–773 (2011).
44. T. L. Delworth, M. E. Mann, *Clim. Dyn.* **16**, 661–676 (2000).
45. R. Zhang, T. L. Delworth, *Geophys. Res. Lett.* **34**, L23708 (2007).
46. R. Zhang, T. L. Delworth, I. M. Held, *Geophys. Res. Lett.* **34**, L02709 (2007).
47. W. T. Welch, K. K. Tung, *J. Atmos. Sci.* **55**, 1285–1302 (1998).

ACKNOWLEDGMENTS

The research of K.-K.T. is supported by NSF under AGS-1262231. X.C. is supported by Natural Science Foundation of China under 41330960 and 41176029. He thanks First Institute of Oceanography of China for its support during his visit to University of Washington. The authors are grateful to many colleagues and the anonymous reviewers who commented on the manuscript and helped improve it. The data sets used in this study are publicly available in http://rda.ucar.edu/datasets/ds285.3/ and https://climatedataguide.ucar.edu/climate-data/oras4-ecmwf-ocean-reanalysis-and-derived-ocean-heat-content.

SUPPLEMENTARY MATERIALS

www.sciencemag.org/content/345/6199/897/suppl/DC1
Materials and Methods
Data
Figs. S1 to S7
Reference (*48*)

17 April 2014; accepted 11 July 2014
10.1126/science.1254937

REPORTS

QUANTUM OPTICS

All-optical routing of single photons by a one-atom switch controlled by a single photon

Itay Shomroni,* Serge Rosenblum,* Yulia Lovsky, Orel Bechler, Gabriel Guendelman, Barak Dayan†

The prospect of quantum networks, in which quantum information is carried by single photons in photonic circuits, has long been the driving force behind the effort to achieve all-optical routing of single photons. We realized a single-photon–activated switch capable of routing a photon from any of its two inputs to any of its two outputs. Our device is based on a single atom coupled to a fiber-coupled, chip-based microresonator. A single reflected control photon toggles the switch from high reflection (R ~ 65%) to high transmission (T ~ 90%), with an average of ~1.5 control photons per switching event (~3, including linear losses). No additional control fields are required. The control and target photons are both in-fiber and practically identical, making this scheme compatible with scalable architectures for quantum information processing.

Photons are a key player in the growing field of quantum information science. The fact that they do not interact with each other has made them ideal for the communication of quantum information yet has prevented so far the realization of deterministic all-optical quantum gates based on single photons. The difficulty to achieve nonlinear behavior at the level of single photons—namely, photon-photon interactions—is considered a major challenge also in the realization of quantum networks, in which quantum information processing

Department of Chemical Physics, Weizmann Institute of Science, Rehovot 76100, Israel.
*These authors contributed equally to this work. **†Corresponding author. E-mail: barak.dayan@weizmann.ac.il**

would be performed by material quantum nodes interconnected by photonic channels (*1*, *2*).

Accordingly, considerable effort has been invested toward the achievement of photon-photon interactions by the mediation of material systems. This effort was pioneered by the attainment of strong coupling between single atoms and optical microresonators in the context of cavity quantum electrodynamics (*3*, *4*), in which the tight confinement of light in tiny volumes leads to drastic enhancement of the electric field associated with each photon in the cavity mode. Antibunching has been observed both with atoms (*5*, *6*) and quantum dots (*7*), and nonlinear phase shifts of 16° (*8*) and recently even π (*9*, *10*) have also been demonstrated with single atoms.

Most notably, based on a scheme that involves auxiliary control fields (*11*), recent works demonstrated nondestructive measurement of an optical photon (*12*), a single-photon phase switch (*9*), and the realization of a quantum gate between flying photons and a single atom, showing atom-photon, photon-photon, and atom-photon-photon entanglement (*13*), all of which can be directly applied to photonic routing.

Nonlinearities such as electromagnetically induced transparency (*14*) and Rydberg blockade (*15*, *16*) have been harnessed for the demonstration of all-optical interactions at lower and lower powers (*17*–*19*). In particular, all-optical switching—in which a weak gate pulse strongly modifies the attenuation of the system—has been demonstrated with very few photons (*20*) and even just one (*21*) photon in the gate pulse. In order to take the next step toward scalable quantum networks, there is a need for switching schemes that coherently route photons between multiple ports in a way that is compatible with large-scale photonic circuits.

Here, we demonstrate the experimental realization of a robust, simple, and scalable scheme for all-optical coherent routing of single photons by single photons, with no need for any additional control fields. Based on a series of theoretical works (*22*–*28*), this scheme uses the mediation of a single, cavity-enhanced, three-level atom in the regime best described as the fast-cavity limit. The same as in the regime of strong-coupling, the coherent coupling rate g between the atom and the cavity mode is larger than both the incoherent loss of the cavity κ_i and the atomic spontaneous emission rate 2γ. Yet in contrast to strong coupling, here the coupling κ_{ex} between the cavity and its input/output modes (the two directions of propagation in the optical fiber, in our case) is the fastest rate in the system, so that a photon emitted by the atom will exit the cavity by coupling to the fiber before the atom could reabsorb it. Accordingly, the dynamics in this regime are best described by the tools of open quantum systems (*29*) and do not include reversible Rabi oscillations between the atom and the cavity mode, but rather irreversible cavity-enhanced spontaneous emission of the atom into the fiber. The crucial parameter in such a system is the cooperativity, or Purcell enhancement factor, $g^2/\kappa\gamma$ (with $\kappa = \kappa_i + \kappa_{ex}$)—namely, the ratio between the atom's cavity-enhanced spontaneous emission rate into the fiber, to the free-space one, which is proportional to the ratio between the cavity's quality factor Q to its mode volume V. Accordingly, by coupling the atom to high-quality (small κ_i) microresonators with tiny mode volumes, it is therefore possible to reach $g^2/\kappa\gamma > 1$, in which case the atom can be assumed to be interacting primarily with the fiber.

The underlying mechanism in our switching scheme is simple and robust and is in fact similar to the interference mechanism that makes metallic mirrors reflect light. The free charges in the mirror oscillate in response to the incoming field and radiate both forward and backward a field that is opposite in phase to the incoming one. The result is destructive interference in the forward direction, which leaves the incoming light no other choice than to be reflected backward. The same effect occurs with a two-level atom in the one-dimensional atom regime: The atom radiates in both directions, and the destructive interference with the incoming probe in the forward direction leads to reflection of the probe backward. The difference between a single atom and a macroscopic mirror is exhibited by the fact that the reflected light in this case is sub-Poissonian because the atom cannot reflect more than one photon at the same instant.

In order to exploit this mechanism for optical switching, one needs to introduce "memory" into the system—namely, a way to make reflection of a single photon toggle the internal state of the atom. This is performed by using a three-level, Λ-type configuration in which the atom has two transitions, each coupled to only one direction of propagation. Such a configuration is depicted in Fig. 1A, where it is assumed that σ^+ polarization propagates only to the right, and σ^- propagates only to the left.

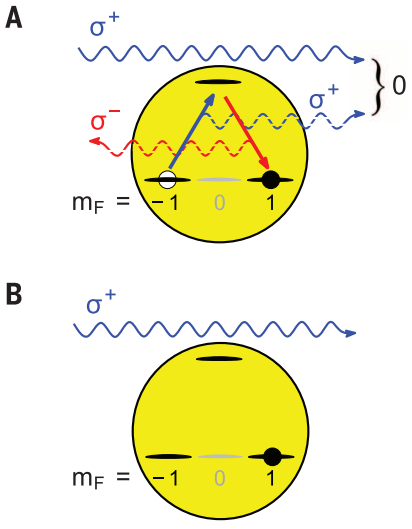

Fig. 1. The two states of the photonic switch. In this three-level atomic Λ-configuration, the σ^+ transition is coupled only to a photonic mode propagating to the right, and the σ^- transition is coupled only to a photonic mode propagating to the left. The atom is irradiated by a σ^+ probe (solid blue wavy arrow). (**A**) For an atom in the $m_F = -1$ ground state, the incoming σ^+ photon will be deterministically reflected as a σ^- photon because of the destructive interference between the probe and the σ^+ emission from the atom (dashed blue wavy arrow), toggling the state of the atom to $m_F = +1$. (**B**) An atom in the $m_F = +1$ ground state does not interact with σ^+ photons, which are accordingly transmitted. The entire scheme is left-right symmetric.

Assuming the initial state of the atom is at $m_F = -1$ and an incoming σ^+ probe, the destructive interference between the probe and the σ^+ field emitted by the atom forces the atom to emit a σ^- photon to the opposite direction, deterministically ending at the $m_F = +1$ state. As a result, any subsequent σ^+ photons will not interact with the atom and will accordingly be transmitted (*27*). Symmetrically, at this stage the system becomes reflective to σ^- photons coming from the right.

This system therefore behaves as a symmetric toggle switch with two inputs, two outputs, and two internal states (Fig. 2A), in which each reflection toggles the internal state. To implement this system as a photonic switch, we use the conventional time-bins protocol and define the first pulse as the control pulse, and the second as the target, which is routed from a certain input to a certain output.

At the heart of our setup is a single ^{87}Rb atom coupled to a chip-based whispering-gallery mode (WGM) silica microsphere resonator (Fig. 2B) (*30*). Light is evanescently coupled to and from the microsphere by a tapered nanofiber, and photons are detected at the outputs by multiple single-photon counting modules (SPCMs). The coupling κ_{ex} between the microsphere and the nanofiber is set by means of careful alignment of their relative position by using a piezo positioning system.

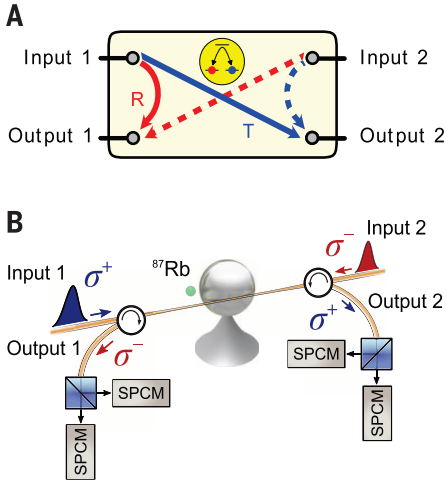

Fig. 2. Schematic of the photonic switch. (**A**) Each input, 1 (solid arrows) or 2 (dashed arrows) may be either transmitted or reflected into one of two outputs, depending on the state of the atom, at $m_F = +1$ (blue) or $m_F = -1$ (red). Each reflection of a single photon toggles the state of the atom. (**B**) The experimental realization of the switch. A single ^{87}Rb atom interacts with a TM WGM resonance of a chip-based silica microsphere resonator. The input-output interface is provided by a tapered optical nanofiber, with the outputs separated from the inputs by optical circulators (*30*). σ^+ modes propagate from left to right, and σ^- modes propagate from right to left. The outputs are delivered to SPCMs.

By working with a transverse-magnetic (TM) mode of the microsphere, we can approximate to a high degree the situation in which σ^+ and σ^- polarizations are coupled to opposite directions. As recently pointed out (*31*), the polarization in the evanescent wave region is very close to σ^+ in one direction, and σ^- in the other, with just ~4% cross-contamination [which naturally leads to some reduction in the efficiency of the switch in this particular realization (*30*)].

The microsphere and the probe were tuned to be resonant with the $F = 1 \rightarrow F' = 0$ transition of the D2 line of ^{87}Rb (Fig. 1). Because atoms in the state $m_F = 0$ barely interact with the TM mode, by choosing this manifold we practically attain the desired Λ-configuration described in Fig. 1, although at the price of decreasing the coherent coupling rate g by a factor of $\sqrt{3}$ compared with the cycling transition ($F = 2 \rightarrow F' = 3$), in which mean $g = 27$ MHz was measured (*30*). To reach the fast cavity limit, we set κ_{ex} to 30 MHz, corresponding to mean $g^2/\kappa\gamma = 2.2$ (*30*).

The rare event of the presence of one atom within the evanescent wave of the TM mode was identified by sending weak (~2.5 photons per pulse) and short [~15 ns full width at half maximum (FWHM)] pulses in the nanofiber in alternating directions and detecting at least three reflected photons within less than 400 ns (*30*). Interleaved between the detection pulses were much weaker (0.24 photons on average in each pulse) and longer (~50 ns FWHM) "target" pulses, whose purpose was to accurately measure the single-photon reflection and transmission properties of the switch. The last detection pulse before each target pulse served as the control, which prepared the atom in a certain initial state. The pulse sequence included control pulses in both directions, preparing the atom half of the times in $m_F = -1$, and half of the times in $m_F = +1$, with the target pulse always polarized σ^+ (*32*).

The measured probabilities for reflection and transmission of the first (and typically the only, if at all) photon in the target pulse are shown in Fig. 3, normalized to the total number of photon detection events (*30*). These are heralded results; namely, they show the statistics of the target pulse conditioned on the detection of one reflected photon in the preceding control pulse.

Specifically, in the cases in which the control pulse was σ^- polarized, detection of a single reflected (σ^+) photon toggled the switch to a state that reflects σ^+ target photons at a probability of 65%. This level is lower than the theoretically expected value of 89% (*30*). We attribute this difference mostly to false events in which the (untrapped) atom was not present in the cavity mode during the entire measurement (*30*).

In cases in which the control pulse was σ^+, detection of a single reflected (σ^-) photon changed the reflection/transmission ratio by a factor of more than 16, leading to ~90% transmission of σ^+ target photons.

To confirm that the toggling of the state is carried out by a single reflection of a control photon, we looked at the normalized probabilities for a second photon detection event in the control pulse. As shown in Fig. 4A, already during the control pulse, after a single reflection the switch becomes highly transmissive, with a probability of only 4.4% to reflect a second photon.

This is a drastic demonstration of single-photon nonlinearity, and as such it is highly nonclassical. Accordingly, the reflected control pulses are antibunched (Fig. 4B), meaning that there is a much larger probability for joint detection of two reflected photons (at different SPCMs) in two unrelated control pulses (from different atom detection events) than within the same control pulse (*30*).

We can therefore conclude that a single reflection of a control photon toggles the state of the atom with high probability. Taking into account the measured probability for such a reflection (~65%), this corresponds to an average of 1.5 control photons per switching event, increasing to ~3 if we include the linear losses in our current realization (which could be practically eliminated by using a higher Q resonance) (*30*).

The potential of this scheme lies in its compatibility with scalable photonic architectures. The device is operated only by the single-photon pulses, which are all in-fiber, identical, and routed to the output ports. This means that a routed target photon can serve as the control photon in the next device, or that the same control photon could activate a few devices. Our demonstration therefore paves the way for the application of this scheme as a versatile, robust, and simple building block for a variety of all-optical photonic devices, from quantum memory (*22*–*24*) through single-photon add/drop filters (*27*), to photonic quantum gates (*24*), all of which being completely passive and compatible with scalable quantum networks.

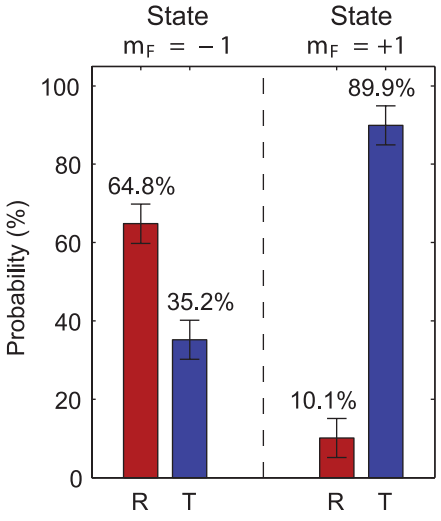

Fig. 3. Single-photon statistics of the photonic switch. In the $m_F = -1$ state, the probability of a σ^+ photon to be reflected is 64.8%, dropping to 10.1% in the $m_F = +1$ state.

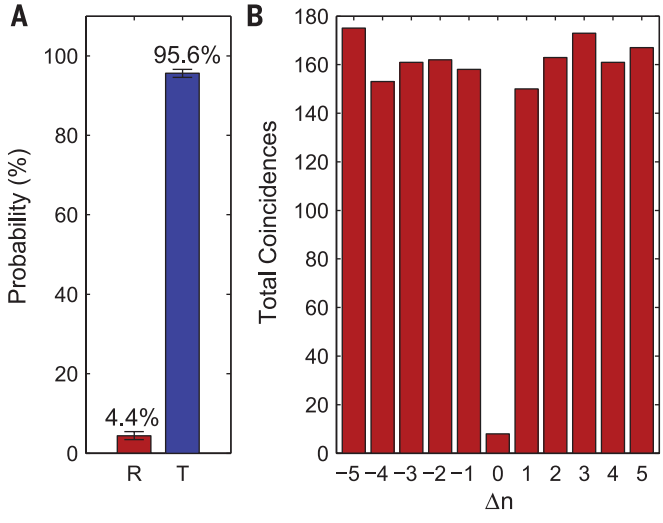

Fig. 4. Single-photon nonlinearity within the control pulse. (**A**) The statistics of the second photon in the control pulse, after the detection of one reflected photon. As shown, the probability of a second reflection drops to 4.4%. (**B**) Antibunching of the reflected control photons, confirming that in most cases only one photon is reflected. For atom-detection events i and j, the total number of coincident detections of two photons in both i and j is shown versus $\Delta n = i - j$. Within the same pulse, the reflection of two photons is accordingly suppressed by a factor of ~20.

REFERENCES AND NOTES

1. J. I. Cirac, P. Zoller, H. J. Kimble, H. Mabuchi, *Phys. Rev. Lett.* **78**, 3221–3224 (1997).
2. H. J. Kimble, *Nature* **453**, 1023–1030 (2008).
3. S. Haroche, J.-M. Raimond, *Exploring the Quantum: Atoms, Cavities, and Photons* (Oxford Univ. Press, New York, 2013).
4. R. J. Thompson, G. Rempe, H. J. Kimble, *Phys. Rev. Lett.* **68**, 1132–1135 (1992).
5. K. M. Birnbaum *et al.*, *Nature* **436**, 87–90 (2005).
6. B. Dayan *et al.*, *Science* **319**, 1062–1065 (2008).
7. D. Press *et al.*, *Phys. Rev. Lett.* **98**, 117402 (2007).
8. Q. A. Turchette, C. J. Hood, W. Lange, H. Mabuchi, H. J. Kimble, *Phys. Rev. Lett.* **75**, 4710–4713 (1995).
9. T. G. Tiecke *et al.*, *Nature* **508**, 241–244 (2014).
10. J. Volz, M. Scheucher, C. Junge, A. Rauschenbeutel, Nonlinear pi phase shift for single fiber-guided photons interacting with a single atom. *arXiv*:1403.1860 (2014).
11. L.-M. Duan, H. J. Kimble, *Phys. Rev. Lett.* **92**, 127902 (2004).
12. A. Reiserer, S. Ritter, G. Rempe, *Science* **342**, 1349–1351 (2013).
13. A. Reiserer, N. Kalb, G. Rempe, S. Ritter, *Nature* **508**, 237–240 (2014).
14. M. Fleischhauer, A. Imamoglu, J. P. Marangos, *Rev. Mod. Phys.* **77**, 633–673 (2005).
15. D. Jaksch *et al.*, *Phys. Rev. Lett.* **85**, 2208–2211 (2000).
16. A. Gaëtan *et al.*, *Nat. Phys.* **5**, 115–118 (2009).
17. A. M. C. Dawes, L. Illing, S. M. Clark, D. J. Gauthier, *Science* **308**, 672–674 (2005).
18. I. Fushman *et al.*, *Science* **320**, 769–772 (2008).
19. T. Peyronel *et al.*, *Nature* **488**, 57–60 (2012).
20. W. Chen *et al.*, *Science* **341**, 768–770 (2013).
21. S. Baur, D. Tiarks, G. Rempe, S. Dürr, *Phys. Rev. Lett.* **112**, 073901 (2014).
22. D. Pinotsi, A. Imamoglu, *Phys. Rev. Lett.* **100**, 093603 (2008).
23. D. E. Chang, A. S. Sørensen, E. A. Demler, M. D. Lukin, *Nat. Phys.* **3**, 807–812 (2007).
24. K. Koshino, S. Ishizaka, Y. Nakamura, *Phys. Rev. A* **82**, 010301 (2010).

25. H. F. Hofmann, K. Kojima, S. Takeuchi, K. Sasaki, . *J. Opt. B* **5**, 218–221 (2003).
26. D. Witthaut, A. S. Sørensen, *New J. Phys.* **12**, 043052 (2010).
27. S. Rosenblum, S. Parkins, B. Dayan, *Phys. Rev. A* **84**, 033854 (2011).
28. J. Gea-Banacloche, W. Wilson, *Phys. Rev. A* **88**, 033832 (2013).
29. H. J. Carmichael, *Phys. Rev. Lett.* **70**, 2273–2276 (1993).
30. Materials and methods are available as supplementary materials on *Science* Online.
31. C. Junge, D. O'Shea, J. Volz, A. Rauschenbeutel, *Phys. Rev. Lett.* **110**, 213604 (2013).
32. We also performed the opposite experiment, in which the control pulses were always σ^-, and the target pulse was half of the times σ^+ and half of the times σ^-. The obtained results were completely consistent with the ones presented here.

ACKNOWLEDGMENTS

Support from the Israeli Science Foundation, the Joseph and Celia Reskin Career Development Chair in Physics, and the Crown Photonics Center is acknowledged. This research was made possible in part by the historic generosity of the Harold Perlman family.

SUPPLEMENTARY MATERIALS

www.sciencemag.org/content/345/6199/903/suppl/DC1
Materials and Methods
Supplementary Text
Figs. S1 to S3
References (*33*, *34*)

11 April 2014; accepted 26 June 2014
Published online 10 July 2014;
10.1126/science.1254699

HELIUM SUPERFLUIDITY

Shapes and vorticities of superfluid helium nanodroplets

Luis F. Gomez,[1]* Ken R. Ferguson,[2] James P. Cryan,[3] Camila Bacellar,[3,4] Rico Mayro P. Tanyag,[1] Curtis Jones,[1] Sebastian Schorb,[2] Denis Anielski,[5,6] Ali Belkacem,[3] Charles Bernando,[7] Rebecca Boll,[5,6,8] John Bozek,[2] Sebastian Carron,[2] Gang Chen,[9]† Tjark Delmas,[10] Lars Englert,[11] Sascha W. Epp,[5,6] Benjamin Erk,[5,6,8] Lutz Foucar,[6,12] Robert Hartmann,[13] Alexander Hexemer,[9] Martin Huth,[13] Justin Kwok,[14] Stephen R. Leone,[3,4,15] Jonathan H. S. Ma,[3,16] Filipe R. N. C. Maia,[17]‡ Erik Malmerberg,[18,19] Stefano Marchesini,[9,20] Daniel M. Neumark,[3,4] Billy Poon,[18] James Prell,[4] Daniel Rolles,[6,8,12] Benedikt Rudek,[5,6]§ Artem Rudenko,[5,6,21] Martin Seifrid,[1] Katrin R. Siefermann,[3]‖ Felix P. Sturm,[3] Michele Swiggers,[2] Joachim Ullrich,[5,6]§ Fabian Weise,[3]¶ Petrus Zwart,[18] Christoph Bostedt,[2,22]# Oliver Gessner,[3]# Andrey F. Vilesov[1,7]#

Helium nanodroplets are considered ideal model systems to explore quantum hydrodynamics in self-contained, isolated superfluids. However, exploring the dynamic properties of individual droplets is experimentally challenging. In this work, we used single-shot femtosecond x-ray coherent diffractive imaging to investigate the rotation of single, isolated superfluid helium-4 droplets containing ~10^8 to 10^{11} atoms. The formation of quantum vortex lattices inside the droplets is confirmed by observing characteristic Bragg patterns from xenon clusters trapped in the vortex cores. The vortex densities are up to five orders of magnitude larger than those observed in bulk liquid helium. The droplets exhibit large centrifugal deformations but retain axially symmetric shapes at angular velocities well beyond the stability range of viscous classical droplets.

The discoveries of superconductors, superfluids, and Bose-Einstein condensates (BECs) (*1*, *2*) reveal that a large number of particles can occupy a single quantum state that extends across macroscopic length scales. A notable example is superfluid ^{4}He (*3*–*6*): It lacks any viscosity below a critical temperature of T_λ = 2.17 K, and its motion is described by a single wave function (*1*, *2*, *5*–*7*). Isolated He nanodroplets were employed to study the onset of superfluidity through the observation of frictionless, quantized rotation of embedded molecules surrounded with varying numbers of ^{4}He atoms (*8*). However, the unambiguous demonstration of a quantum mechanical state of motion of an entire helium nanodroplet remains challenging.

In a finite droplet, any manifestation of liquid flow must involve rotational motion, which, in a superfluid, embodies itself in quantum vortices (*6*, *7*). Indeed, the formation of regular arrays of parallel vortices was detected in a rotating bucket filled with superfluid He (*9*, *10*). However, surprisingly little is known about quantum rotation in superfluid droplets. Calculations predict that vortices may exist in ^{4}He droplets as small as a few nanometers in diameter (*11*–*13*), but experimental studies of this elusive phenomenon remain challenging (*14*). Recently, traces of vortices were detected in He droplets ~1 μm in diameter (*15*). However, these exploratory experiments did not provide detailed hydrodynamic properties of the spinning droplets, such as their shapes or the spatial arrangements of the vortices they contain. In this work, we studied the rotation of single, isolated superfluid He nanodroplets via coherent scattering of x-rays from a free-electron laser (FEL) (*16*–*18*). Figure 1 illustrates the experiment, in which ^{4}He droplets with radii R = 100 to 1000 nm [number of He atoms (N_{He}) = 10^8 to 10^{11}] were produced upon fragmentation of liquid helium expanding into a vacuum (*15*, *19*, *20*) [see section S1 of (*21*)]. After a time of flight of 3.8 ms across a distance of 640 mm from the nozzle, the droplets traversed the focus of the FEL beam [photon energy = 1.5 keV, wavelength λ = 0.827 nm]. Diffraction images were recorded with a pn-junction charge-coupled device detector placed ≈565 mm behind the interaction volume. Each image originates from a single droplet irradiated by a single FEL shot. The low-density core of ^{4}He vortices is ≈0.2 nm in diameter (*7*), which does not provide sufficient contrast for direct detection by x-ray scattering. Therefore, the droplets are doped with Xe atoms ($N_{Xe} \approx 10^{-3} N_{He}$), which cluster along the vortex cores (*10*, *15*) and act as a contrast agent.

Diffraction images of individual neat helium droplets are shown in Fig. 2, A to C. The circular and elliptical diffraction contours in Fig. 2, A and B, are consistent with diffraction from spheroidal droplets with a symmetry half-axis a and two equal perpendicular half-axes b (fig. S2). The aspect ratio AR = (long half-axis)/(short half-axis)

[1]Department of Chemistry, University of Southern California (USC), Los Angeles, CA 90089, USA. [2]Linac Coherent Light Source (LCLS), SLAC National Accelerator Laboratory, 2575 Sand Hill Road, Menlo Park, CA 94025, USA. [3]Ultrafast X-ray Science Laboratory, Chemical Sciences Division, Lawrence Berkeley National Laboratory (LBNL), Berkeley, CA 94720, USA. [4]Department of Chemistry, University of California Berkeley, Berkeley, CA 94720, USA. [5]Max-Planck-Institut für Kernphysik, Saupfercheckweg 1, 69117 Heidelberg, Germany. [6]Max Planck Advanced Study Group at the Center for Free-Electron Laser Science (CFEL), Notkestraße 85, 22607 Hamburg, Germany. [7]Department of Physics and Astronomy, USC, Los Angeles, CA 90089, USA. [8]Deutsches Elektronen-Synchrotron (DESY), Notkestraße 85, 22607 Hamburg, Germany. [9]Advanced Light Source, LBNL, Berkeley, CA 94720, USA. [10]CFEL, DESY, Notkestraße 85, 22607 Hamburg, Germany. [11]Max-Planck-Institut für Extraterrestrische Physik, Giessenbachstraße, 85741 Garching, Germany. [12]Max-Planck-Institut für Medizinische Forschung, Jahnstrasse 29, 69120 Heidelberg, Germany. [13]PNSensor GmbH, Otto-Hahn-Ring 6, 81739 München, Germany. [14]Mork Family Department of Chemical Engineering and Materials Science, USC, Los Angeles, CA 90089, USA. [15]Department of Physics, University of California Berkeley, Berkeley, CA 94720, USA. [16]Department of Physics, The Chinese University of Hong Kong, Hong Kong, China. [17]National Energy Research Scientific Computing Center, LBNL, Berkeley, CA 94720, USA. [18]Physical Biosciences Division, LBNL, Berkeley, CA 94720, USA. [19]Department of Plant and Microbial Biology, University of California Berkeley, Berkeley, CA 94720, USA. [20]Department of Physics, University of California Davis, Davis, CA 95616, USA. [21]James R. Macdonald Laboratory, Department of Physics, Kansas State University, Manhattan, KS 66506, USA. [22]PULSE Institute, Stanford University and SLAC National Accelerator Laboratory, 2575 Sand Hill Road, Menlo Park, CA 94025, USA.
*Present address: New Focus, 3635 Peterson Way, Santa Clara, CA 95054, USA. †Present address: Shanghai Synchrotron Radiation Facility, Shanghai Institute of Applied Physics, Chinese Academy of Sciences, Shanghai 201204, China. ‡Present address: Department of Cell and Molecular Biology, Uppsala University, Husargatan 3, Uppsala 75124, Sweden. §Present address: Physikalisch-Technische Bundesanstalt, Bundesallee 100, D-38116 Braunschweig, Germany. ||Present address: Leibniz Institute of Surface Modification (IOM), Permoserstraße 15, 04318 Leipzig, Germany. ¶Present address: Berliner Glas KGaA Herbert Kubatz GmbH, Waldkraiburger Straße 5, 12347 Berlin, Germany.
#Corresponding author. E-mail: bostedt@slac.stanford.edu (C.B.); ogessner@lbl.gov (O.G.); vilesov@usc.edu (A.F.V.)